Buckling or vibration Galerkin modes for bistable curved beam dynamics: which yields acceptable convergence?

Zhuhuan Wu
School of Aeronautic Science and Engineering,
Beihang University,
Beijing 100191, China
e-mail: wzh2405422@buaa.edu.cn

Ke Huang
School of Aeronautic Science and Engineering,
Beihang University,
Beijing 100191, China
e-mail: huangke@buaa.edu.cn

Jiaying Zhang[1]
School of Aeronautic Science and Engineering,
Beihang University,
Beijing 100191, China
e-mail: jiaying.zhang@buaa.edu.cn

ABSTRACT

Dynamic excitation enables rapid state switching of bistable beams under small forcing amplitudes, yet a controllable switching strategy relies on accurate prediction of beam dynamics. The Galerkin method offers a reliable and efficient approach, but the choice of trial functions varies across studies, leaving the optimal selection for both efficiency and accuracy unresolved. This paper investigates three most commonly used modal sets for a bistable curved beam: straight-beam buckling modes, straight-beam vibration modes, and curved-beam vibration modes. Substituting these trial functions into the governing equation with increasing truncation orders, we numerically compute and compare the dynamic response patterns. One-mode and two-mode truncations yield similar patterns across the three sets but fail to fully capture the primary

[1] Corresponding author.

resonance and main harmonic regions. The three-mode truncation, however, reveals significant discrepancies in the subharmonic inter-well region between the buckling modes and the two vibration modes. These discrepancies arise from the axial force effects included in the buckling problem but neglected in the vibration problems, a mechanism substantiated by an axial-to-bending energy ratio analysis. This indicates faster convergence of the buckling modes, which is confirmed by the five-mode results, where all predictions converge and agree qualitatively with the three-mode buckling predictions. Finite element simulations and a parametric study further validate these findings. The study demonstrates that the buckling modes exhibit superior convergence and that a five-mode truncation is generally required to capture the full dynamics, providing a clear and reasoned basis for selecting trial functions and truncation order for bistable curved beams.

Keywords: Galerkin method, bistable curved beam, buckling mode shapes, vibration mode shapes, nonlinear dynamics, convergence

1. Introduction

Bistable structures, characterized by two distinct stable equilibrium states, offer a compelling paradigm for reconciling the inherent trade-off between large deformability and low static power consumption [1,2]. Unlike conventional linear systems, they require no persistent external energy to maintain either configuration [3]. This unique attribute has spurred their extensive adoption in advanced applications ranging from reconfigurable metamaterials [4,5] and shape-morphing actuators [3,6], to microelectromechanical systems (MEMS) [7] and broadband energy harvesters [8,9].

Among the diverse forms of bistable structures, the bistable beam stands out as the most fundamental one-dimensional element. Owing to its structural simplicity and well-defined mechanics [10,11], it serves as an ideal platform for revealing the nonlinear dynamic behaviors inherent to bistable structures. Bistable beams generally fall into two categories: buckled beams and pre-shaped curved beams. A buckled beam is typically realized by applying axial compression to an initially straight beam, leading to elastic buckling that produces two laterally symmetric stable equilibria [12,13]. In contrast, the pre-shaped curved beam derives its bistability from an initial geometric curvature, thus eliminating the need for external prestressing. This not only simplifies both fabrication and assembly, but also facilitates micro-scale integration [14,15]. As a result, the curved beam has attracted considerable research attention in recent years. For instance, Ueno et al. [16] integrated bistable curved beams into a frequency conversion interposer for a MEMS vibration energy harvester to enhance power generation efficiency. By tuning the geometric parameters of the curved beam, the threshold acceleration required to trigger snap-through can be adjusted, enabling the system to respond effectively to various ambient vibration frequencies. The output energy can be increased up to 1.69 times, demonstrating the effectiveness of this approach in energy harvesting. Huang et al. [17] proposed a single-actuator bistable microdevice. By pushing different rods to apply moments for state transitions, the device can remain in either stable state without any latching mechanism. Experiments demonstrated reliable switching at a maximum rate of approximately 40 Hz with an actuation voltage of 10 V. Zhang et al. [18] combined two curved beams in parallel to form a unit cell for a metastructure. By leveraging the bistability of the curved beams and tuning the geometric parameters, the unit cell can achieve either translational or rotational stable states. This provides a promising strategy for designing adaptive structures capable of large rotations and translations.

To achieve controllable switching between the two stable states, classical methods mainly rely on quasi-static loading [19]. However, this approach often suffers from a large critical switching force and slow response [20]. Recent research has therefore turned to dynamic excitation strategies [21,22]. Bonthron and Tubaldi [23] applied the Galerkin method to investigate the frequency response and steady-state behavior of both hinged-hinged shallow buckled beams and curved beams under harmonic lateral excitation. Their results, particularly when truncating to the third mode, revealed that inter-well motion can occur even under relatively small forcing amplitudes near the first natural frequency of the linearized system around equilibria. This implies that, by applying harmonic or other time-varying excitations and leveraging the inertial and resonance properties of bistable systems to induce dynamic instability, the required excitation amplitude for snap-through can be significantly reduced [20,24]. Consequently, swift and efficient state switching becomes feasible, laying a theoretical foundation for high-performance smart actuation systems.

The realization of dynamic excitation strategies, however, hinges on the accurate prediction of bistable system dynamics. The Galerkin method, as one of the classical and efficient approaches for solving distributed-parameter system dynamics [25], offers a practical route toward this goal. As a prominent member of the weighted residual methods, it typically adopts identical trial and test functions to reduce the governing partial differential equations to a finite set of ordinary differential equations. To ensure convergence under high-order truncation, the trial functions need to be selected from a complete set of orthogonal functions [26]. Yet, the question of how to choose trial functions that simultaneously achieve rapid convergence and maintain high accuracy in practical problems remains open. Classically, trial functions are chosen as the eigenfunctions of the linearized system, as this enables convenient equation decoupling and substantially simplifies the computation. In the context of curved beam dynamics, the eigenfunctions are typically the vibration mode shapes of either a straight beam or the curved beam itself [27]. Xiao et al. [28,29] adopted curved-beam vibration modes as trial functions in the Galerkin reduction of the dynamic equation for MEMS arch beams. By studying the reduced equations truncated to the first order, they investigated the synchronization time and the dual-jump property of the beam, respectively. Ouakad and Younis [30] examined the convergence behavior of these two sets of vibration modes by evaluating the static displacement of MEMS curved beam structures. Their results showed negligible discrepancy between the two sets at the fifth truncation order, where both had already converged, yet the straight-beam vibration modes incurred a much lower computational cost. This finding subsequently motivated the adoption of straight-beam vibration modes in their later work [31,32]. Apart from vibration modes, some researchers have instead adopted the buckling modes of a straight beam to reduce the dynamic equations of bistable beams, a choice particularly well-studied for capturing their force-displacement relationships and snap-through characteristics [33-35]. Hasan et al. [20], for example, employed the buckling modes as trial functions in a Galerkin discretization of the buckled beam’s dynamical equation. By truncating to the first mode and solving the resulting system numerically, they revealed how a static bias force reshapes the parameter region of dynamic excitation for switching behaviors, thereby controlling the reliable operating space. Wu et al. [36] adopted the first buckling mode within the Galerkin framework to systematically explore how gravity and initial curvature affect the symmetry-breaking dynamic behavior of the curved beam, with both numerical and analytical predictions validated through experiments. This divergence in practice once again raises a key question: which set of trial functions can deliver both fast convergence and accurate dynamic predictions under low-order truncation for a bistable system? For bistable curved beams specifically, the question thus boils down to a systematic comparison among three candidate sets of trial functions: the straight-beam vibration mode shapes, the curved-beam vibration mode shapes, and the straight-beam buckling mode shapes.

Moreover, the truncation order in the Galerkin method significantly influences the accuracy of the predicted beam dynamics. For pinned-pinned bistable beams, Bonthron and Tubaldi [23] numerically computed the steady-state response using single-mode and three-mode Galerkin truncations, respectively. The significant discrepancies between these results clearly demonstrate the necessity of higher-order truncations to fully capture the dynamic behavior. Librandi et al. [37] expanded the lateral displacement of pinned-pinned bistable beams using sine-series modes to study their snap-through properties, and found that the numerical results converged after the third-mode truncation, which was subsequently validated by experimental measurements. For clamped-clamped beams, however, the convergence requirements can differ. Ouakad and Younis [30] demonstrated that a five-mode truncation is required for acceptable convergence in calculating the static deflection of a shallow MEMS arch. The same truncation order was adopted for their subsequent dynamic analysis, although a dedicated convergence study for the dynamic case was not performed. Furthermore, Chen et al. [38] proposed two schemes, based on the natural frequencies of the corresponding linear conservative system, to determine the convergent truncation order for beams on elastic foundations. However, the applicability of these schemes to clamped-clamped bistable beams has not been verified. Together, these observations highlight the need to identify a suitable truncation order for converged dynamic predictions of bistable curved beams.

In this paper, a sinusoidal pre-shaped curved beam is adopted to investigate the dynamic behavior patterns and convergence properties associated with three commonly used sets of Galerkin trial functions. The governing equation is discretized via the Galerkin method, and the steady-state responses are computed numerically using each set at increasing truncation order and mapped onto the same parameter plane of forcing amplitude and frequency for direct comparison. The results reveal discrepancies among the different trial function sets and truncation orders, yet all converge at a five-mode truncation. These discrepancies are traced to the distinct physical considerations underlying the buckling and vibration problems. Finite element simulations confirm the accuracy of the converged Galerkin predictions, and a parametric study demonstrates that the conclusions hold under varied geometric and damping conditions. This paper provides researchers with a clear and reasoned basis for selecting appropriate trial functions and truncation orders when analyzing bistable beam dynamics. The remainder of the paper is organized as follows: Section 2 formulates the dynamical model and derives the discretized equations; Section 3 presents and compares the numerical results for ascending truncation orders; Section 4 provides the finite element validation and parametric study; and Section 5 summarizes the conclusions.

2. Dynamic analysis and Galerkin discretization

2.1. Dynamic model of the curved beam

Consider a homogeneous curved beam with span *L*, width *b* and thickness *c*, subjected to clamped-clamped boundary conditions, as shown in Fig. 1. The beam has a constant cross-sectional area *A*, moment of inertia $I = bc^3/12$, and an initial stress-free profile $\hat{w}_0(\hat{x}) = -h/2 \cdot [1 - \cos(2\pi\hat{x}/L)]$, where *h* denotes the initial arch height. The material properties are defined by the density *ρ* and Young's modulus *E*. The beam is oriented vertically with its arch directed upward, and its own weight acts as a uniformly distributed load, with $\hat{g}$ representing the gravitational acceleration. Under a harmonic distributed excitation, the equation of motion for the lateral displacement $\hat{w}(\hat{x}, \hat{t})$ is given by [37]

$$
\begin{aligned}
&\rho A\left(\frac{\partial^2 \hat{w}}{\partial \hat{t}^2} - \hat{g}\right) + \hat{C}_{\mathrm{d}}\frac{\partial \hat{w}}{\partial \hat{t}} + EI\left(\frac{\partial^4 \hat{w}}{\partial \hat{x}^4} - \frac{\partial^4 \hat{w}_0}{\partial \hat{x}^4}\right) \\
&- \frac{EA}{2L}\left\{\int_0^L \left[\left(\frac{\partial \hat{w}}{\partial \hat{x}}\right)^2 - \left(\frac{\partial \hat{w}_0}{\partial \hat{x}}\right)^2\right] \mathrm{d}\hat{x}\right\}\frac{\partial^2 \hat{w}}{\partial \hat{x}^2} = \hat{f}\cos(\hat{\Omega}\hat{t})
\end{aligned}
\tag{1}
$$

where $\hat{C}_{\mathrm{d}}$ is the damping coefficient, $\hat{f}$ and $\hat{\Omega}$ are the excitation amplitude and angular frequency, respectively.

Introducing the nondimensional parameters as follows:

$$
\begin{gathered}
w=\frac{\widehat{w}}{h}, \qquad w_0=\frac{\widehat{w}_0}{h}, \qquad t=\frac{\hat{t}}{T}, \qquad x=\frac{\hat{x}}{L}, \qquad T=\sqrt{\frac{\rho A L^4}{EI}}, \\
g=\frac{T^2}{h}\hat{g}, \qquad Q=\frac{h}{c}, \qquad C_{\mathrm{d}}=\frac{\hat{C}_{\mathrm{d}}L^2}{\sqrt{\rho AEI}}, \qquad f=\frac{\hat{f}L^4}{EIh}
\end{gathered}
\tag{2}
$$

Equation (1) can therefore be transformed into

$$
\begin{gathered}
\left(\frac{\partial^2 w}{\partial t^2}-g\right)+C_{\mathrm{d}}\frac{\partial w}{\partial t}+\left(\frac{\partial^4 w}{\partial x^4}-\frac{\partial^4 w_0}{\partial x^4}\right) \\
-6Q^2\left\{\int_0^1\left[\left(\frac{\partial w}{\partial x}\right)^2-\left(\frac{\partial w_0}{\partial x}\right)^2\right]\mathrm{d}x\right\}\frac{\partial^2 w}{\partial x^2}=f\cos\left(\hat{\Omega}Tt\right)
\end{gathered}
\tag{3}
$$

2.2. Galerkin discretization

Equation (3) is then solved using the Galerkin truncation method, where the nondimensional displacement $w(x,t)$ is expressed as a linear combination of trial functions $\phi_i(x)$ with corresponding generalized displacements $q_i(t)$:

$$
w(x,t)=\sum_{i=1}^{n}q_i(t)\phi_i(x) \tag{4}
$$

Substituting Eq. (4) into Eq. (3) yields the following discretized equation:

$$\left(\sum_{i=1}^{n}\phi_i\frac{\mathrm{d}^2q_i}{\mathrm{d}t^2}-g\right)+C_\mathrm{d}\sum_{i=1}^{n}\phi_i\frac{\mathrm{d}q_i}{\mathrm{d}t}+\left(\sum_{i=1}^{n}\frac{\mathrm{d}^4\phi_i}{\mathrm{d}x^4}q_i-\frac{\mathrm{d}^4\phi_0}{\mathrm{d}x^4}\right)$$

$$-6Q^2\left\{\int_0^1\left[\sum_{i=1}^{n}\left(\frac{\mathrm{d}\phi_i}{\mathrm{d}x}\right)^2q_i^2+2\sum_{1\le i<k\le n}^{n}\frac{\mathrm{d}\phi_i}{\mathrm{d}x}\frac{\mathrm{d}\phi_k}{\mathrm{d}x}q_iq_k\right.\right. \tag{5}$$

$$\left.\left.-\left(\frac{\mathrm{d}\phi_0}{\mathrm{d}x}\right)^2\right]\mathrm{d}x\right\}\left(\sum_{i=1}^{n}\frac{\mathrm{d}^2\phi_i}{\mathrm{d}x^2}q_i\right)=f\cos\left(\hat{\Omega}Tt\right)$$

where

$$\phi_0(x)=w_0(x)=-\frac{1}{2}[1-\cos(2\pi x)] \tag{6}$$

By multiplying both sides of Eq. (5) by ϕ_j and then integrating from 0 to 1, the equation can be rewritten as

$$\sum_{i=1}^{n}M_{ji}\frac{\mathrm{d}^2q_i}{\mathrm{d}t^2}+C_\mathrm{d}\sum_{i=1}^{n}M_{ji}\frac{\mathrm{d}q_i}{\mathrm{d}t}+\left(\sum_{i=1}^{n}K_{ji}q_i+6Q^2A_0\sum_{l=1}^{n}B_{jl}q_l\right)-S_j-F_jg$$

$$-6Q^2\left(\sum_{i=1}^{n}A_iq_i^2+2\sum_{1\le i<k\le n}^{n}C_{ik}q_iq_k\right)\left(\sum_{l=1}^{n}B_{jl}q_l\right)=F_jf\cos\left(\hat{\Omega}Tt\right), \tag{7}$$

$$j=1,2,\cdots,n$$

where

$$M_{ji}=\int_0^1\phi_i\phi_j\,\mathrm{d}x,\qquad K_{ji}=\int_0^1\frac{\mathrm{d}^4\phi_i}{\mathrm{d}x^4}\phi_j\,\mathrm{d}x,\qquad A_0=\int_0^1\left(\frac{\mathrm{d}\phi_0}{\mathrm{d}x}\right)^2\mathrm{d}x,$$

$$F_j=\int_0^1\phi_j\,\mathrm{d}x,\qquad S_j=\int_0^1\frac{\mathrm{d}^4\phi_0}{\mathrm{d}x^4}\phi_j\,\mathrm{d}x,\qquad A_i=\int_0^1\left(\frac{\mathrm{d}\phi_i}{\mathrm{d}x}\right)^2\mathrm{d}x, \tag{8}$$

$$B_{jl}=\int_0^1\frac{\mathrm{d}^2\phi_l}{\mathrm{d}x^2}\phi_j\,\mathrm{d}x,\qquad C_{ik}=\int_0^1\frac{\mathrm{d}\phi_i}{\mathrm{d}x}\frac{\mathrm{d}\phi_k}{\mathrm{d}x}\mathrm{d}x\quad(i<k)$$

Note that the operations of integration and summation are interchangeable for a finite discretisation order n and continuous trial function $\phi_i(x)$ on [0,1].

As introduced in the Introduction, we consider three commonly used types of trial functions for curved beams: the buckling mode shapes of straight beams (hereinafter simply "buckling mode shapes" for brevity), the vibration mode shapes of straight beams, and the vibration mode shapes of curved beams. Their explicit expressions are given as follows.

For the buckling mode shapes, we have

$$\phi_i^{\mathrm{b}}(x) = \begin{cases} \dfrac{1}{2}[1-\cos(N_i x)] & N_i = (i+1)\pi, \qquad i = 1,3,\cdots \\ \dfrac{1}{2}\left[1-2x-\cos(N_i x)+\dfrac{2\sin(N_i x)}{N_i}\right] & N_i = 2.86\pi, 4.92\pi,\cdots \quad i = 2,4,\cdots \end{cases} \tag{9}$$

The vibration mode shapes of straight beams are expressed as

$$\phi_i^{\mathrm{sv}}(x) = \cos\beta_i x - \cosh\beta_i x - \frac{\cos\beta_i - \cosh\beta_i}{\sin\beta_i - \sinh\beta_i}(\sin\beta_i x - \sinh\beta_i x) \tag{10}$$

where β_i is governed by

$$\cos\beta_i \cosh\beta_i = 1 \tag{11}$$

The vibration mode shapes of curved beams take the form [27]

$$\begin{aligned}\phi_i^{\mathrm{cv}}(x) = c_{i1}\sin\sqrt{\alpha_i}x + c_{i2}\cos\sqrt{\alpha_i}x + c_{i3}\sinh\sqrt{\alpha_i}x + c_{i4}\cosh\sqrt{\alpha_i}x \\ + c_{i5}\cos 2\pi x\end{aligned} \tag{12}$$

where the coefficients c_{ij} (j = 1,2,…,5) and the parameter α_i satisfy

$$\begin{cases} c_{i2}+c_{i4}+c_{i5}=0 \\ c_{i1}+c_{i3}=0 \\ c_{i1}\sin\sqrt{\alpha_i}+c_{i2}\cos\sqrt{\alpha_i}+c_{i3}\sinh\sqrt{\alpha_i}+c_{i4}\cosh\sqrt{\alpha_i}+c_{i5}=0 \\ c_{i1}\cos\sqrt{\alpha_i}-c_{i2}\sin\sqrt{\alpha_i}+c_{i3}\cosh\sqrt{\alpha_i}+c_{i4}\sinh\sqrt{\alpha_i}=0 \\ \sqrt{\omega}\begin{bmatrix} c_{i1}\langle\bar{\phi}_0'\cos\sqrt{\alpha_i}x\rangle-c_{i2}\langle\bar{\phi}_0'\sin\sqrt{\alpha_i}x\rangle \\ +c_{i3}\langle\bar{\phi}_0'\cosh\sqrt{\alpha_i}x\rangle+c_{i4}\langle\bar{\phi}_0'\sinh\sqrt{\alpha_i}x\rangle \end{bmatrix}+c_{i5}\left(\frac{\omega^2}{2\pi^2}-9\pi^2\right)=0 \end{cases} \tag{13}$$

Here, the angle brackets denote the inner product $\langle f(x)g(x)\rangle=\int_0^1 f(x)g(x)\mathrm{d}x$, and the reference initial shape is defined as $\bar{\phi}_0(x)=|\phi_0(x)|=[1-\cos(2\pi x)]/2$. These trial functions inherently satisfy the clamped-clamped boundary conditions. For bistable curved beams, to facilitate comparison of dynamic responses obtained using different trial functions, time is rescaled based on a common reference frequency as

$$\tau=\omega_{\mathrm{ref}}t \quad \Rightarrow \quad t=\frac{\tau}{\omega_{\mathrm{ref}}} \tag{14}$$

where

$$\omega_{\mathrm{ref}}=\sqrt{-\frac{K_{11}^{\mathrm{b}}+6Q^2A_0B_{11}^{\mathrm{b}}}{M_{11}^{\mathrm{b}}}}=2\pi^2\sqrt{\frac{3Q^2-4}{3}} \tag{15}$$

in which K_{11}^{b}, B_{11}^{b}, and M_{11}^{b} are coefficients derived from the buckling mode shapes $\phi_i^{\mathrm{b}}(x)$. It follows from Eq. (15) that the system possesses bistability only when Q is greater than $2\sqrt{3}/3$.

Substituting Eq. (14) into Eq. (7) leads to

$$\sum_{i=1}^{n}M_{ji}\ddot{q}_i+\delta\sum_{i=1}^{n}M_{ji}\dot{q}_i+\sum_{i=1}^{n}\widetilde{K}_{ji}q_i-\tilde{S}_j-\tilde{F}_jg-N_j(\mathbf{q})=\tilde{F}_jf\cos(\omega\tau), \quad j=1,2,\cdots,n \tag{16}$$

where

$$\delta = \frac{C_\mathrm{d}}{\omega_\mathrm{ref}}, \qquad \widetilde{K}_{ji} = \frac{K_{ji} + 6Q^2 A_0 B_{ji}}{\omega_\mathrm{ref}^2}, \qquad \tilde{S}_j = \frac{S_j}{\omega_\mathrm{ref}^2},$$
$$\tilde{F}_j = \frac{F_j}{\omega_\mathrm{ref}^2}, \qquad \omega = \frac{\hat{\Omega} T}{\omega_\mathrm{ref}}, \tag{17}$$
$$N_j(\mathbf{q}) = \frac{6Q^2}{\omega_\mathrm{ref}^2}\left(\sum_{i=1}^{n} A_i q_i^2 + 2\sum_{1\le i<k\le n} C_{ik} q_i q_k\right)\left(\sum_{l=1}^{n} B_{jl} q_l\right),$$
$$\mathbf{q} = (q_1, q_2, \cdots, q_n)^\mathrm{T}$$

and the overdot denotes differentiation with respect to time τ. Equation (16) reveals that the system dynamics are governed by several key components: the coupling effect of the mass matrix, the linear and nonlinear stiffness terms, and constant biases arising from the initial curvature and gravitational force. Moreover, by choosing the first buckling mode shape as the reference, the nondimensional forcing amplitude is defined as

$$F = \frac{F_1^\mathrm{b} f}{M_{11}^\mathrm{b} \omega_\mathrm{ref}^2} \quad \Rightarrow \quad f = \frac{M_{11}^\mathrm{b} \omega_\mathrm{ref}^2}{F_1^\mathrm{b}} F \tag{18}$$

where F_1^b denotes the coefficient obtained from the first buckling mode shape. Substituting Eq. (18) into Eq. (16) yields

$$\sum_{i=1}^{n} M_{ji}\ddot{q}_i + \delta \sum_{i=1}^{n} M_{ji}\dot{q}_i + \sum_{i=1}^{n} \widetilde{K}_{ji} q_i - \tilde{S}_j - \tilde{F}_j g - N_j(\mathbf{q}) = \gamma_j F\cos(\omega\tau), \tag{19}$$
$$j = 1,2,\cdots,n$$

where

$$\gamma_j = \frac{M_{11}^\mathrm{b}}{F_1^\mathrm{b}} F_j \tag{20}$$

Equation (19) can also be written in vector form as

$$\mathbf{M}\ddot{\mathbf{q}} + \delta\mathbf{M}\dot{\mathbf{q}} + \widetilde{\mathbf{K}}\mathbf{q} - \tilde{\mathbf{S}} - g\tilde{\mathbf{F}} - \mathbf{N}(\mathbf{q}) = F\boldsymbol{\Gamma}\cos(\omega\tau) \tag{21}$$

where

$$\mathbf{M} = \left[M_{ji}\right]_{n\times n}, \qquad \widetilde{\mathbf{K}} = \left[\widetilde{K}_{ji}\right]_{n\times n}, \qquad \tilde{\mathbf{S}} = \left(\tilde{S}_1, \tilde{S}_2, \cdots, \tilde{S}_n\right)^{\mathrm{T}},$$
$$\tilde{\mathbf{F}} = \left(\tilde{F}_1, \tilde{F}_2, \cdots, \tilde{F}_n\right)^{\mathrm{T}}, \qquad \mathbf{N}(\mathbf{q}) = \left(N_1(\mathbf{q}), N_2(\mathbf{q}), \cdots, N_n(\mathbf{q})\right)^{\mathrm{T}}, \tag{22}$$
$$\mathbf{\Gamma} = (\gamma_1, \gamma_2, \cdots, \gamma_n)^{\mathrm{T}}$$

Equation (21) [or (19)] is now in the form suitable for numerical computation in the parameter space of forcing amplitude F and frequency ω, enabling the comparison of dynamic responses derived from various trial functions up to any desired order n. The initial condition is defined as $\mathbf{q_0} = (q_{10}, q_{20}, \ldots, q_{n0})^{\mathrm{T}}$, which satisfies the following equation when time derivatives and external force in Eq. (21) are set to zero:

$$\widetilde{\mathbf{K}}\mathbf{q_0} - \tilde{\mathbf{S}} - g\tilde{\mathbf{F}} - \mathbf{N}(\mathbf{q_0}) = \mathbf{0} \tag{23}$$

3. Numerical analysis

3.1. Low-order truncation

With the governing equations established, we now proceed to numerical analysis. Following the classification and criteria established in [20,24], the beam's dynamic responses are categorized into four types:

(1) Switching: The vibration starts from one stable state, transitions to the other, and never returns to the initial state;

(2) Reverting: The system also undergoes inter-well motion from the initial equilibrium to the other, but ultimately returns to the initial stable state and never jumps again;

(3) Vacillating: The system continuously switches back and forth between the two stable states without settling into either one;

(4) Intra-well: The system vibrates solely around the initial stable state and never transitions to the other potential well.

The first three types are collectively referred to as inter-well motions due to their well-crossing behavior. To determine the steady-state motion type, we compare the mid-point displacement during vibration with the saddle displacement, which indicates whether the system has transitioned to the other potential well.

Before performing dynamic simulations, we first examine the mode shapes of the three trial function sets to gain an intuitive impression of their differences. Using the parameter values listed in Table 1 and the expressions given in Eqs. (9)–(13), we plot the first three mode shapes of each set in Fig. 2, each normalized by its maximum value. The figure reveals that the first two mode shapes are highly similar across all three sets. For the third mode, however, the buckling-mode shape clearly deviates from the two vibration-mode shapes, suggesting that discrepancies may arise when the truncation order reaches three. In contrast, the straight-beam and curved-beam vibration mode shapes remain nearly identical across all three orders.

We begin the dynamic analysis with a single-mode truncation, which also serves to capture the essential dynamic characteristics of the curved beam. Setting the truncation order to $n = 1$ and employing the parameters in Table 1, the dynamic responses in the (ω,F) plane are computed using the fourth-order Runge-Kutta method, as shown in Fig. 3. The forcing amplitude F ranges from 0.03 to 0.60, and the angular frequency ω

ranges from 0.2 to 3.0, covering the main resonance region as well as the primary superharmonics and subharmonics.

The results in Fig. 3 show that the inter-well motion region exhibits multiple self-similar V-shaped patterns in the (ω,F) plane. Within each V-shaped region lies a smaller, similarly V-shaped central area corresponding to vacillating motion for the primary resonance and superharmonics. In the main resonance region, feather-shaped areas where switching and reverting motions are intermingled are observed flanking the right boundary of its vacillating region [24]. The subharmonics region, located at approximately twice the frequency of the primary resonance tip, requires a sufficiently large forcing amplitude to trigger inter-well motion. The figure also demonstrates the high similarity between the dynamic responses obtained using the buckling, straight-beam vibration, and curved-beam vibration mode shapes when the truncation order is set to n = 1.

The truncation order is further extended to n = 2, which includes the asymmetric mode ϕ_2. Similarly, the dynamic responses are computed using the three sets of trial functions and presented in Fig. 4. The results again show high similarity between the three mode shapes, but deviate from those obtained with the first-order truncation (Fig. 3). Although the frequencies at the tips of the inter-well region generally align with the first-order results, the required forcing amplitude decreases significantly, particularly for the superharmonics. Within the inter-well region for ω < 2.0, vacillating motion dominates, while switching and reverting motions are confined to narrow bands near the boundary. The minimum forcing amplitude remains largely unchanged at low forcing frequencies, but increases dramatically after ω = 1.5, forming a sharp right boundary of this region.

The subharmonics region retains its V-shaped structure, with all four motion types interwoven.

3.2. High-order truncation

To accurately capture the effects of strong nonlinearity and fully predict the complete dynamics of the curved beam, high-order truncation is required. Using the same numerical method to solve Eq. (19), the system's dynamic responses are computed for a truncation order of $n = 3$, with the results shown in Fig. 5.

Figure 5 reveals similar dynamic responses between all three sets of trial functions at low forcing frequencies, for both upper and lower initial states. However, discrepancies appear at high frequencies ($1.9 < \omega < 2.5$) and large forcing amplitude ($0.3 < F < 0.6$). In this region, when the motion is initiated from the upper stable state, all three mode sets predict V-shaped inter-well regions. However, the region predicted by the buckling modes is significantly larger, exhibiting a lower tip forcing amplitude and a wider frequency range under a given amplitude, while the two vibration mode shapes yield nearly identical results. Conversely, when initiated from the lower stable state, the buckling modes yield a distinct V-shaped vacillating region, whereas both straight-beam and curved-beam vibration modes produce switching behavior in the tip region, forming a W-shaped vacillating region above.

Moreover, a comparison of the results for truncation order $n = 3$ with those for lower orders ($n = 1,2$) reveals that the dependence of the dynamic patterns on the initial state becomes significantly more pronounced at higher order. At this higher truncation order, the system tends to vibrate around the lower stable state at low forcing frequencies ($0.2 < \omega < 0.6$) and small forcing amplitudes, and around the upper stable state at relatively high frequencies ($1.0 < \omega < 2.2$) and large amplitudes. Consequently, when initiating from the upper stable state, the dynamic responses exhibit switching behavior followed by intra-well motion as the forcing frequency and amplitude increase. In contrast, when starting from the lower stable state, the system exhibits intra-well motion followed by switching behavior in the corresponding parameter regions. Under lower-order truncations, however, the system displays similar dynamic behavior in the same parameter regions irrespective of the initial state, as shown in Fig. 3 and Fig. 4.

Given the discrepancies between the three sets of modal results at high forcing frequencies and large amplitudes, we seek to determine which provides more accurate predictions. To this end, we increase the truncation order to $n = 5$ and compute the dynamic response patterns in the (ω,F) plane, as shown in Fig. 6. The results reveal broadly similar dynamic response patterns across all three mode sets over the studied parameter plane. More importantly, within the region where discrepancies were previously observed, all three mode sets now exhibit a scattered inter-well region when the motion is initiated from the upper stable state. Although this region does not fully coincide with the one obtained using buckling modes at $n = 3$ [Fig. 5(a)], the lower-order prediction still captures the inter-well motion qualitatively, with the tip occurring at comparable forcing frequencies and amplitudes. This indicates that the buckling modes converge faster than both vibration mode sets in solving the curved beam dynamics. Specifically, a third-order truncation using the buckling modes is already sufficient to qualitatively capture the main resonance as well as the primary superharmonics and subharmonics, whereas the vibration modes require a higher-order truncation (e.g., fifth-order) to achieve comparable performance.

Furthermore, for all three mode sets, the dynamic behavior patterns at low forcing frequencies ($0.2 < \omega < 1.7$) agree well with the third-order truncation results in Fig. 5. This confirms that a third-order truncation is largely sufficient to accurately predict the system's primary resonance behavior in the (ω,F) plane.

While the fifth-order truncation results validate the accuracy of the third-order approximation, a key question remains: why do the dynamic behavior patterns at high forcing frequencies differ between the buckling modes and the vibration modes? These discrepancies can be intuitively attributed to the marked difference between the third-order mode shape of the buckling modes and those of the vibration modes, as illustrated in Fig. 2. This difference, in turn, stems from the distinct governing equations that define the buckling and vibration problems, respectively. Specifically, the buckling mode shapes defined in Eq. (9) are obtained by solving

$$EI\frac{\mathrm{d}^4 w}{\mathrm{d}x^4} + P\frac{\mathrm{d}^2 w}{\mathrm{d}x^2} = 0 \tag{24}$$

under clamped-clamped boundary conditions, where P denotes the axial force. In contrast, the straight-beam vibration mode shapes defined in Eq. (10) are derived from

$$\rho A\frac{\partial^2 w}{\partial t^2} + EI\frac{\partial^4 w}{\partial x^4} = 0 \tag{25}$$

under the same boundary conditions, in which the axial force is not considered. As for the curved-beam vibration mode shapes defined in Eq. (12), although their derivation accounts for the initial curvature of the beam, it also neglects axial inertia and assumes that the axial displacement is entirely induced by the lateral motion [27]. Consequently, they share the same fundamental simplification as the straight-beam vibration modes. The governing equation (1) of the beam dynamics, however, contains a nonlinear term that originates from axial tension/compression, which governs the overall system dynamics. This term reveals the effect of axial force on the lateral dynamics. Due to the relatively shallow geometry of the curved beam (c/L = 0.087), the conclusion for straight beams, namely that the axial resonance frequency is higher than the lateral one [39,40], can be reasonably extended to the present case. Therefore, under high-frequency excitation, the influence of axial vibration becomes significant, suggesting that the buckling modes, which incorporate the coupled transverse-axial effect, may capture the true dynamic behavior at high frequencies. Consequently, the system's dynamic responses could be accurately predicted even with a low-order truncation. In contrast, the vibration modes consider only lateral motion, which may lead to distortion in the computed dynamic responses under low-order truncation. Furthermore, the shallow geometry, together with the shared simplification principles, explains the near-perfect overlap of the straight-beam and curved-beam mode shapes shown in Fig. 2, as well as the high similarity of their dynamic response patterns at each truncation order.

To further validate the explanation regarding the role of axial force, we quantify its significance in terms of the relative energetic contributions of axial versus bending deformation during the steady-state response. Specifically, we compute the ratio of the average axial (tension/compression) potential energy $\overline{U}_{\mathrm{s}}$ to the average bending potential energy $\overline{U}_{\mathrm{b}}$. A larger value of this ratio indicates a comparatively more important role of axial force relative to bending. Following the detailed derivation presented in Appendix A, this energy ratio is evaluated numerically over the (ω,F) plane for a truncation order of n = 3. The results are presented in Fig. 7.

Figure 7 reveals two regions with a large axial-to-bending energy ratio for both initial states. Of these two regions, the one located at low forcing frequencies shows good agreement among the three sets of trial functions, whereas the one at high frequencies exhibits a clear discrepancy between the predictions by the buckling modes and those by the vibration modes. Specifically, when the motion starts from the upper stable state, the high-frequency region forms a “<”-shaped feature, whose tip possesses the largest energy ratio and is located close to the tip of the V-shaped inter-well region in Figs. 5(a)–(c). Therefore, in agreement with the V-shaped pattern, the forcing amplitude at the “<”-shaped tip computed using the buckling modes is significantly smaller than that obtained using the vibration modes. For all choices of mode shapes, moreover, the lower boundary of this high-frequency region coincides with the extension of the left boundary of the V-shaped region, while the upper boundary generally aligns with the right boundary of the V-shaped region. Within the “<”-shaped region, the energy ratio decreases radially from the tip toward the high-frequency side. The results for the lower initial state exhibit similar characteristics, albeit with a more scattered lower boundary compared to the sharp boundary observed in the upper-state case.

These findings demonstrate that the axial force plays a significant role at the tip of the “<”-shaped region, thereby influencing the exact location of the V-shaped inter-well region. Consequently, incorporating axial force effects into the trial functions is crucial for reduced-order models to faithfully capture the true dynamics of the system. This validates the rationality of the previous discussion and confirms the superior performance of buckling mode shapes in predicting steady-state responses.

4. Validation and parametric study

4.1. Finite element validation

To validate the accuracy of the analytical predictions, a finite element model is constructed in Abaqus 2024. The geometry is generated directly from the initial shape function $\hat{w}_0(\hat{x})$ with the parameters listed in Table 1, and the corresponding material properties are assigned. Mass-proportional Rayleigh damping is adopted with a coefficient $\alpha = \hat{C}_\mathrm{d}/\rho A \approx 18.48\ \mathrm{s}^{-1}$, matching the viscous damping coefficient $\hat{C}_\mathrm{d}$ used in the theoretical model. Both ends are fully clamped, and the beam is subjected to gravity together with a uniformly distributed harmonic excitation. An implicit dynamic analysis is performed with geometric nonlinearity enabled, and the mid-point displacement is recorded to identify the steady-state motion type according to the same classification criterion applied to the Galerkin results.

Figure 8(a) superimposes the finite element predictions (circular and diamond-shaped markers) for motions initiated from the upper stable state onto the background of the fifth-order buckling-mode Galerkin results. To examine the convergence of the fifth-order truncation more closely, additional simulation points are placed in the subharmonic resonance region indicated by the red dashed frame. The finite element results agree well with the Galerkin predictions, confirming both the correctness of the numerical model and the convergence of the fifth-order Galerkin solution.

To further verify the role of the axial force that underlies the faster convergence of the buckling modes, the time-averaged ratio of axial potential energy to bending potential energy is also evaluated from the finite element simulations. The bending and axial energies are computed from the sectional moment $\widehat{M}(\hat{x},\hat{t})$ and axial force $\widehat{N}(\hat{x},\hat{t})$, integrated along the beam and averaged over a steady-state time interval:

$$\frac{\overline{U}_{\mathrm{s}}}{\overline{U}_{\mathrm{b}}}=\frac{\int_{\hat{t}_1}^{\hat{t}_2}\int_0^L \dfrac{\widehat{N}^2(\hat{x},\hat{t})}{2EA}\,\mathrm{d}\hat{x}\,\mathrm{d}\hat{t}}{\int_{\hat{t}_1}^{\hat{t}_2}\int_0^L \dfrac{\widehat{M}^2(\hat{x},\hat{t})}{2EI}\,\mathrm{d}\hat{x}\,\mathrm{d}\hat{t}} \tag{26}$$

Here $[\hat{t}_1,\hat{t}_2]$ is a time window after the steady state has been reached. Figure 8(b) plots these simulated energy ratios (dotted markers) against the background of the fifth-order buckling-mode numerical results for motions initiated from the upper stable state. Similar to the third-order results in Figs. 7(a)–(c), both the numerical and finite element results exhibit a distinct region of elevated energy ratio beneath the subharmonic vacillating zone, as highlighted by the red dashed frame. This agreement confirms the significant contribution of the axial force in this region, which explains why the buckling modes—being derived from a problem that intrinsically includes axial force effects—achieve a faster convergence than the vibration modes. The consistency between the finite element and numerical results further corroborates the validity of the proposed Galerkin framework.

4.2. Parametric study

The preceding analysis relies on a specific set of parameter values. To assess the generality of the conclusions, we vary the initial arch height *h* and the viscous damping coefficient $\hat{C}_{\mathrm{d}}$ independently. Figure 9 shows the dynamic responses for *h* = 4.50 mm

(0.177 in), while Fig. 10 presents the corresponding results for $\hat{C}_d$ = 0.15 Pa·s (3.13×10^{-3} lbf·s/ft^2). All cases are initiated from the upper stable state and computed using third-order and fifth-order truncations with each of the three trial function sets.

Consistent with the earlier findings, the fifth-order results from all three mode sets converge to broadly the same response patterns in both figures. The buckling modes again exhibit superior convergence: their third-order predictions of the subharmonic region—both its extent and its tip forcing amplitude—match the converged fifth-order results more closely than those obtained with either set of vibration modes. This confirms that the conclusions drawn from the reference parameter set hold under the varied geometric and damping conditions considered here. In addition, the findings can be extended to the base-excitation case through an equivalent force transformation, whereas changes in boundary conditions or geometric slenderness would require modifying the trial functions or the beam model. Although such extensions lie beyond the scope of the present study, they represent worthwhile directions for future work.

5. Conclusions

This study investigates the convergence properties of three sets of trial functions, namely the straight-beam buckling modes, the straight-beam vibration modes, and the curved-beam vibration modes, in predicting the dynamic responses of a bistable curved beam. Numerical results show that a single-mode truncation captures the basic inter-well motion regions, and adding the second mode markedly lowers the predicted forcing amplitude required for inter-well motion at low forcing frequencies. Despite highly similar low-order patterns across the three mode sets, these truncations fail to fully capture the primary resonance as well as the main superharmonics and subharmonics. At third order, significant discrepancies appear between the buckling modes and the two vibration modes in the subharmonic inter-well region. These discrepancies are traced to the different physical considerations governing the mode shapes: buckling modes inherently include axial force effects, whereas both vibration mode sets neglect them. An energy-based analysis, comparing the ratio of the averaged axial potential energy to the averaged bending energy, confirms that the axial force plays a decisive role near the tip of this subharmonic region, thereby supporting the higher accuracy of the buckling-mode predictions. This inference is corroborated by the five-mode truncation results, as the results from all three sets of trial functions converge to broadly the same response patterns, and the tip frequencies of the inter-well region agree closely with that obtained using the third-order buckling truncation. This agreement also confirms that the buckling modes already yield qualitatively accurate predictions at the third order and converge appreciably faster. Independent finite element simulations further validate these findings, with both the steady-state response patterns and the axial-to-bending energy ratios matching the converged fifth-order results. A parametric study demonstrates that these conclusions hold across different initial arch heights and viscous damping levels.

Taken together, these findings demonstrate that the buckling modes, by incorporating axial force effects into lateral dynamics, are better suited than the vibration modes for predicting the main dynamic properties of bistable curved beams. Meanwhile, owing to the shallow geometry of the beam and the shared simplification of neglecting axial force effects, the two sets of vibration modes exhibit high similarity in both mode shapes and dynamic behaviors at each truncation order. The study further indicates that a five-mode truncation is generally required to fully capture the primary dynamic responses of the bistable curved beam. Overall, this work provides a clear physical rationale for selecting Galerkin trial functions and truncation orders for bistable curved beams, with potential implications for similar studies on bistable plates, shells, and three-dimensional structures.

Acknowledgment

This project has received funding from National Natural Science Foundation of China (Grant No. 92271104, 12102017) and Beijing Natural Science Foundation (Grant No. 1232014).

Conflict of Interest

There are no conflicts of interest.

Data Availability Statement

The datasets generated and supporting the findings of this article are obtainable from the corresponding author upon reasonable request.

Appendix A Derivation of the axial-to-bending energy ratio

Based on the parameters and coordinate definitions introduced in Section 2.1, the bending potential energy of the curved beam is given by

$$\widehat{U}_{\mathrm{b}} = \frac{1}{2} EI \int_0^L \left(\frac{\partial^2 \widehat{w}}{\partial \hat{x}^2} - \frac{\partial^2 \widehat{w}_0}{\partial \hat{x}^2} \right)^2 \mathrm{d}\hat{x} \tag{A1}$$

Introducing the nondimensional quantities from Eq. (2) transforms this expression into

$$\widehat{U}_{\mathrm{b}} = \frac{EIh^2}{2L^3} \int_0^1 \left(\frac{\partial^2 w}{\partial x^2} - \frac{\partial^2 w_0}{\partial x^2} \right)^2 \mathrm{d}x \tag{A2}$$

The lateral displacement is then expanded according to the discretization scheme in Eq. (4), leading to

$$\widehat{U}_{\mathrm{b}} = \frac{EIh^2}{2L^3} \int_0^1 \left(\sum_{i=1}^{n} q_i \frac{\mathrm{d}^2 \phi_i}{\mathrm{d}x^2} - \frac{\mathrm{d}^2 \phi_0}{\mathrm{d}x^2} \right)^2 \mathrm{d}x \tag{A3}$$

Expanding the integrand and exchanging the orders of summation and integration yields

$$\begin{aligned}\widehat{U}_{\mathrm{b}} = \frac{EIh^2}{2L^3} \Bigg[& \sum_{i=1}^{n} \sum_{j=1}^{n} q_i q_j \int_0^1 \frac{\mathrm{d}^2 \phi_i}{\mathrm{d}x^2} \frac{\mathrm{d}^2 \phi_j}{\mathrm{d}x^2} \mathrm{d}x - 2 \sum_{i=1}^{n} q_i \int_0^1 \frac{\mathrm{d}^2 \phi_i}{\mathrm{d}x^2} \frac{\mathrm{d}^2 \phi_0}{\mathrm{d}x^2} \mathrm{d}x \\ & + \int_0^1 \left(\frac{\mathrm{d}^2 \phi_0}{\mathrm{d}x^2} \right)^2 \mathrm{d}x \Bigg]\end{aligned} \tag{A4}$$

For notational brevity, we define

$$\begin{gathered}[\mathbf{K}_{\mathrm{b}}]_{ij} = \int_0^1 \frac{\mathrm{d}^2 \phi_i}{\mathrm{d}x^2} \frac{\mathrm{d}^2 \phi_j}{\mathrm{d}x^2} \mathrm{d}x, \qquad (\mathbf{f}_{\mathrm{b}})_i = \int_0^1 \frac{\mathrm{d}^2 \phi_i}{\mathrm{d}x^2} \frac{\mathrm{d}^2 \phi_0}{\mathrm{d}x^2} \mathrm{d}x, \\ c_{\mathrm{b}} = \int_0^1 \left(\frac{\mathrm{d}^2 \phi_0}{\mathrm{d}x^2} \right)^2 \mathrm{d}x\end{gathered} \tag{A5}$$

The bending potential energy then condenses to the compact quadratic form

$$\widehat{U}_{\mathrm{b}} = \frac{EIh^2}{2L^3}\left(\mathbf{q}^{\mathrm{T}}\mathbf{K}_{\mathrm{b}}\mathbf{q} - 2\mathbf{f}_{\mathrm{b}}^{\mathrm{T}}\mathbf{q} + c_{\mathrm{b}}\right) \tag{A6}$$

We now turn to the axial (tension/compression) potential energy. During vibration, the length change of the beam is approximated by

$$\begin{aligned}\Delta\hat{s} &\approx \int_0^L \left[1 + \frac{1}{2}\left(\frac{\partial\widehat{w}}{\partial\hat{x}}\right)^2\right]\mathrm{d}\hat{x} - \int_0^L \left[1 + \frac{1}{2}\left(\frac{\partial\widehat{w}_0}{\partial\hat{x}}\right)^2\right]\mathrm{d}\hat{x} \\ &= \frac{1}{2}\int_0^L \left[\left(\frac{\partial\widehat{w}}{\partial\hat{x}}\right)^2 - \left(\frac{\partial\widehat{w}_0}{\partial\hat{x}}\right)^2\right]\mathrm{d}\hat{x}\end{aligned} \tag{A7}$$

The associated axial potential energy is therefore

$$\widehat{U}_{\mathrm{s}} = \frac{1}{2}\frac{EA}{L}(\Delta\hat{s})^2 = \frac{EA}{8L}\left\{\int_0^L \left[\left(\frac{\partial\widehat{w}}{\partial\hat{x}}\right)^2 - \left(\frac{\partial\widehat{w}_0}{\partial\hat{x}}\right)^2\right]\mathrm{d}\hat{x}\right\}^2 \tag{A8}$$

Applying the nondimensionalization (2) produces the dimensionless counterpart

$$\widehat{U}_{\mathrm{s}} = \frac{EAh^4}{8L^3}\left\{\int_0^1 \left[\left(\frac{\partial w}{\partial x}\right)^2 - \left(\frac{\partial w_0}{\partial x}\right)^2\right]\mathrm{d}x\right\}^2 \tag{A9}$$

Inserting the modal expansion (4) gives

$$\widehat{U}_{\mathrm{s}} = \frac{EAh^4}{8L^3}\left\{\int_0^1 \left[\left(\sum_{i=1}^{n} q_i\frac{\mathrm{d}\phi_i}{\mathrm{d}x}\right)^2 - \left(\frac{\mathrm{d}\phi_0}{\mathrm{d}x}\right)^2\right]\mathrm{d}x\right\}^2 \tag{A10}$$

Interchanging summation and integration once more results in

$$\widehat{U}_{\mathrm{s}} = \frac{EAh^4}{8L^3}\left\{\sum_{i=1}^{n}\sum_{j=1}^{n} q_i q_j \int_0^1 \frac{\mathrm{d}\phi_i}{\mathrm{d}x}\frac{\mathrm{d}\phi_j}{\mathrm{d}x}\,\mathrm{d}x - \int_0^1 \left(\frac{\mathrm{d}\phi_0}{\mathrm{d}x}\right)^2\mathrm{d}x\right\}^2 \tag{A11}$$

Introducing the auxiliary quantities

$$[\mathbf{G}_{\mathrm{s}}]_{ij} = \int_0^1 \frac{\mathrm{d}\phi_i}{\mathrm{d}x}\frac{\mathrm{d}\phi_j}{\mathrm{d}x}\,\mathrm{d}x\,, \qquad c_{\mathrm{s}} = \int_0^1 \left(\frac{\mathrm{d}\phi_0}{\mathrm{d}x}\right)^2\mathrm{d}x \tag{A12}$$

allows the axial potential energy to be written concisely as

$$\widehat{U}_{\mathrm{s}} = \frac{EAh^4}{8L^3}\left(\mathbf{q}^{\mathrm{T}}\mathbf{G}_{\mathrm{s}}\mathbf{q} - c_{\mathrm{s}}\right)^2 \tag{A13}$$

To evaluate the energy ratio under steady-state conditions, we first compute the time-averaged values of the axial and bending potential energies separately, and then take their ratio. This yields

$$\frac{\overline{U}_{\mathrm{s}}}{\overline{U}_{\mathrm{b}}} = \frac{\frac{1}{T}\int_{\tau_1}^{\tau_2}\widehat{U}_{\mathrm{s}}\mathrm{d}\tau}{\frac{1}{T}\int_{\tau_1}^{\tau_2}\widehat{U}_{\mathrm{b}}\mathrm{d}\tau} = 3Q^2\frac{\int_{\tau_1}^{\tau_2}\left(\mathbf{q}^{\mathrm{T}}\mathbf{G}_{\mathrm{s}}\mathbf{q} - c_{\mathrm{s}}\right)^2\mathrm{d}\tau}{\int_{\tau_1}^{\tau_2}\left(\mathbf{q}^{\mathrm{T}}\mathbf{K}_{\mathrm{b}}\mathbf{q} - 2\mathbf{f}_{\mathrm{b}}^{\mathrm{T}}\mathbf{q} + c_{\mathrm{b}}\right)\mathrm{d}\tau} \tag{A14}$$

where τ_1 and τ_2 are two nondimensional time instants chosen after the system has attained a steady state, and $T = \tau_2 - \tau_1$ is the corresponding time span.

REFERENCES

[1] Cao, Y., Derakhshani, M., Fang, Y., Huang, G., and Cao, C., 2021, "Bistable structures for advanced functional systems," Adv. Funct. Mater., **31**(45), 2106231. DOI: 10.1002/adfm.202106231

[2] Xu, R., Chen, C., Sun, J., He, Y., Lu, M.-H., and Chen, Y., 2023, "The design, manufacture and application of multistable mechanical metamaterials-a state-of-the-art review," Int. J. Extreme Manuf., **5**(4), 042013. DOI: 10.1088/2631-7990/acf96a

[3] Chi, Y., Li, Y., Zhao, Y., Hong, Y., Tang, Y., and Yin, J., 2022, "Bistable and multistable actuators for soft robots: Structures, materials, and functionalities," Adv. Mater., **34**(19), 2110384. DOI: 10.1002/adma.202110384

[4] Jiao, P., Mueller, J., Raney, J. R., Zheng, X., and Alavi, A. H., 2023, "Mechanical metamaterials and beyond," Nat. Commun., **14**, 6004. DOI: 10.1038/s41467-023-41679-8

[5] Chen, T., Pauly, M., and Reis, P. M., 2021, "A reprogrammable mechanical metamaterial with stable memory," Nature, **589**, pp. 386–390. DOI: 10.1038/s41586-020-03123-5

[6] Hu, N., Li, B., Bai, R., Xie, K., and Chen, G., 2023, "A torsion-bending antagonistic bistable actuator enables untethered crawling and swimming of miniature robots," Research, **6**, 0116. DOI: 10.34133/research.0116

[7] Huang, S.-W., Lin, F.-C., and Yang, Y.-J., 2020, "A novel single-actuator bistable microdevice with a moment-driven mechanism," Sens. Actuators A, **310**, 111934. DOI: 10.1016/j.sna.2020.111934

[8] Zhou, S., Lallart, M., and Erturk, A., 2022, "Multistable vibration energy harvesters: Principle, progress, and perspectives," J. Sound Vib., **528**, 116886. DOI: 10.1016/j.jsv.2022.116886

[9] Derakhshani, M., Momenzadeh, N., and Berfield, T. A., 2021, "Analytical and experimental study of a clamped-clamped, bistable buckled beam low-frequency PVDF vibration energy harvester," J. Sound Vib., **497**, 115937. DOI: 10.1016/j.jsv.2021.115937

[10] Yan, S., Wu, L., Wen, Y., Sun, J., and Zhou, J., 2025, "Snap-through instability in mechanical metamaterials," Responsive Mater., **3**(1), e20240035. DOI: 10.1002/rpm.20240035

[11] Huang, K., Zhang, J., Huang, W., Wang, Q., Shaw, A.D., and Friswell, M.I., 2026, "Exploring sequential snapping bifurcation through a tunable energy landscape," Phys. Rev. Applied, **25**(6), 064029. DOI: 10.1103/nxpg-92kv

[12] Zhao, Y., Fang, H., Diao, B., Zhang, X., and Xu, J., 2023, "Exploiting the bistable dynamics in a two-module vibration-driven robot for locomotion performance enhancement," J. Sound Vib., **544**, 117387. DOI: 10.1016/j.jsv.2022.117387

[13] Pan, D., Wu, Z., Dai, F., and Tolou, N., 2020, "A novel design and manufacturing method for compliant bistable structure with dissipated energy feature," Mater. Des., **196**, 109081. DOI: 10.1016/j.matdes.2020.109081

[14] Hussein, H., Khan, F., and Younis, M. I., 2020, "A symmetrical bistable mechanism from combination of pre-shaped microbeams," Sens. Actuators A, **306**, 111961. DOI: 10.1016/j.sna.2020.111961

[15] Hussein, H., Khan, F., and Younis, M. I., 2020, "A monolithic tunable symmetric bistable mechanism," Smart Mater. Struct., **29**(7), 075033. DOI: 10.1088/1361-665X/ab8ea3

[16] Ueno, H., Toshiyoshi, H., and Suzuki, T., 2024, "Frequency conversion interposer with no-internal stress curved-beam for MEMS vibrational energy harvesters," Sens. Actuators A, **378**, 115750. DOI: 10.1016/j.sna.2024.115750

[17] Huang, S.-W., Lin, F.-C., and Yang, Y.-J., 2020, "A novel single-actuator bistable microdevice with a moment-driven mechanism," Sens. Actuators A, **310**, 111934. DOI: 10.1016/j.sna.2020.111934

[18] Zhang, Y., Tichem, M., and van Keulen, F., 2021, "Rotational snap-through behavior of multi-stable beam-type metastructures," Int. J. Mech. Sci., **193**, 106172. DOI: 10.1016/j.ijmecsci.2020.106172

[19] Qiu, J., Lang, J. H., and Slocum, A. H., 2004, "A curved-beam bistable mechanism," J. Microelectromech. Syst., **13**(2), pp. 137–146. DOI: 10.1109/JMEMS.2004.825308

[20] Hasan, M. N., Paul, S., Greenwood, T. E., Parker, R. G., Kong, Y. L., and Wang, P., 2025, "Harmonically induced shape morphing of bistable buckled beam with static bias," Extrem. Mech. Lett., **76**, 102299. DOI: 10.1016/j.eml.2025.102299

[21] Zhang, J., Wu, Z., Zhang, C., Hao, L., Nie, R., and Qiu, J., 2019, "Nonlinear dynamics of shape memory alloys actuated bistable beams," Smart Mater. Struct., **28**(5), 055009. DOI: 10.1088/1361-665X/ab0325

[22] Mao, J., Gao, W., Liu, C., Cao, D., and Lai, S., 2025, "Transition analysis of meta-stable and bi-stable nonlinear behavior in piezoelectric vibration energy harvesting through a pre-shaped curved beam model," Appl. Math. Mech.-Engl. Ed., **46**(11), pp. 2017–2034. DOI: 10.1007/s10483-025-3319-6

[23] Bonthron, M., and Tubaldi, E., 2024, "Dynamic behavior of bistable shallow arches: from intrawell to chaotic motion," J. Appl. Mech., **91**(2), 021010. DOI: 10.1115/1.4064208

[24] Hasan, M. N., Greenwood, T. E., Parker, R. G., Kong, Y. L., and Wang, P., 2023, "Fractal patterns in the parameter space of a bistable Duffing oscillator," Phys. Rev. E, **108**(2), L022201. DOI: 10.1103/PhysRevE.108.L022201

[25] Li, H.-X., and Qi, C., 2010, "Modeling of distributed parameter systems for applications—A synthesized review from time–space separation," J. Process Control, **20**(8), pp. 891–901. DOI: 10.1016/j.jprocont.2010.06.016

[26] Nayfeh, A H., and Pai, P. F., 2004, *Linear and nonlinear structural mechanics*, John Wiley & Sons, Weinheim, Germany, Chap. 1. ISBN: 978-0-471-59356-0

[27] Lacarbonara, W., and Rega, G., 2003, "Resonant non-linear normal modes. Part II: activation/orthogonality conditions for shallow structural systems," Int. J. Non Linear Mech., **38**(6), pp. 873–887. DOI: 10.1016/S0020-7462(02)00034-3

[28] Xiao, Z., Shi, Z., Lv, Q., Wang, X., Wei, X., and Huan, R., 2025, "Optimized synchronization efficiency in micromechanical arch beams," Int. J. Mech. Sci., **291–292**, 110098. DOI: 10.1016/j.ijmecsci.2025.110098

[29] Xiao, Z., Shi, Z., Wang, X., Wei, X., and Huan, R., 2024, "Dual-jump amplification in an electric-thermal adjusted arch beam micro-resonator," Sens. Actuators A, **365**, 114925. DOI: 10.1016/j.sna.2023.114925

[30] Ouakad, H. M., and Younis, M. I., 2010, "The dynamic behavior of MEMS arch resonators actuated electrically," Int. J. Non Linear Mech., **45**(7), pp. 704–713. DOI: 10.1016/j.ijnonlinmec.2010.04.005

[31] Ouakad, H. M., and Younis, M. I., 2014, "On using the dynamic snap-through motion of MEMS initially curved microbeams for filtering applications," J. Sound Vib., **333**(2), pp. 555–568. DOI: 10.1016/j.jsv.2013.09.024

[32] Alkharabsheh, S. A., and Younis, M. I., 2013, "Statics and dynamics of MEMS arches under axial forces," J. Vib. Acoust., **135**(2), 021007. DOI: 10.1115/1.4023055

[33] Li, P. Q., Wang, Y. S., Wang, K. F., and Wang, B. L., 2025, "An elastic-boundary-controlled framework for on-demand stability switching in bistable curved beam metamaterials," Int. J. Solids Struct., **320**, 113542. DOI: 10.1016/j.ijsolstr.2025.113542

[34] Hua, J., Zhou, Y., and Chen, C. Q., 2024, "Design and analysis of a tunable multistable mechanical metamaterial," Int. J. Mech. Sci., **272**, 109170. DOI: 10.1016/j.ijmecsci.2024.109170

[35] Hua, J., Zhou, Y., Meng, Z., and Chen, C. Q., 2025, "Pre-compressed beam-based multistable mechanical metamaterials with programmable loading and unloading deformation sequences," Thin-Walled Struct., **209**, 112879. DOI: 10.1016/j.tws.2024.112879

[36] Wu, Z., Huang, K., Wang, N., Huang, W., Wang, Q., and Zhang, J., 2026, "Analysis of nonlinear dynamics of a curved beam under gravity bias," Phys. Rev. E, **114**(1), 015501. DOI: 10.1103/nxxl-x79n

[37] Librandi, G., Tubaldi, E., and Bertoldi, K., 2020, "Snapping of hinged arches under displacement control: Strength loss and nonreciprocity," Phys. Rev. E, **101**(5), 053004. DOI: 10.1103/PhysRevE.101.053004

[38] Chen, H.-Y., Ding, H., Li, S.-H., and Chen, L.-Q., 2020, "Convergent term of the Galerkin truncation for dynamic response of sandwich beams on nonlinear foundations," J. Sound Vib., **483**, 115514. DOI: 10.1016/j.jsv.2020.115514

[39] Timoshenko, S. P., 1937, *Vibration Problems in Engineering*, second ed., D. Van Nostrand Company, New York, USA, Chap. 6.

[40] Tse, F. S., Morse, I. E., and Hinkle, R. T., 2004, *Mechanical Vibrations: Theory and Applications*, second ed., CBS Publishers & Distributors, New Delhi, India, Chap. 7. ISBN: 978-93-879-6458-7

Figure Captions List

Fig. 1 Schematic of a clamped-clamped curved beam with its geometric parameters and under harmonic distributed excitation

Fig. 2 Comparison of the first three buckling mode shapes (dashed lines), straight-beam vibration mode shapes (solid lines), and curved-beam vibration mode shapes (dotted lines), each normalized by its maximum value. In the main plot, the straight-beam and curved-beam vibration mode shapes are barely distinguishable. The inset provides a magnified view of the region where they diverge, highlighting the subtle difference between the straight- and curved-beam vibration modes.

Fig. 3 Dynamic responses of the curved beam computed by the Galerkin method with truncation order n = 1. The six subfigures correspond to different initial states and trial functions: (a) upper stable state, buckling modes ($\phi = \phi^{b}$); (b) upper stable state, straight beam vibration modes ($\phi = \phi^{sv}$); (c) upper stable state, curved beam vibration modes ($\phi = \phi^{cv}$); (d) lower stable state, buckling modes ($\phi = \phi^{b}$); (e) lower stable state, straight beam vibration modes ($\phi = \phi^{sv}$); (f) lower stable state, curved beam vibration modes ($\phi = \phi^{cv}$).

Fig. 4 Dynamic responses of the curved beam computed by the Galerkin method with truncation order n = 2. The six subfigures correspond to different initial states and trial functions: (a) upper stable state, buckling modes (ϕ

= ϕ^b); (b) upper stable state, straight beam vibration modes (ϕ = ϕ^{sv}); (c) upper stable state, curved beam vibration modes (ϕ = ϕ^{cv}); (d) lower stable state, buckling modes (ϕ = ϕ^b); (e) lower stable state, straight beam vibration modes (ϕ = ϕ^{sv}); (f) lower stable state, curved beam vibration modes (ϕ = ϕ^{cv}).

Fig. 5 Dynamic responses of the curved beam computed by the Galerkin method with truncation order n = 3. The six subfigures correspond to different initial states and trial functions: (a) upper stable state, buckling modes (ϕ = ϕ^b); (b) upper stable state, straight beam vibration modes (ϕ = ϕ^{sv}); (c) upper stable state, curved beam vibration modes (ϕ = ϕ^{cv}); (d) lower stable state, buckling modes (ϕ = ϕ^b); (e) lower stable state, straight beam vibration modes (ϕ = ϕ^{sv}); (f) lower stable state, curved beam vibration modes (ϕ = ϕ^{cv}).

Fig. 6 Dynamic responses of the curved beam computed by the Galerkin method with truncation order n = 5. The six subfigures correspond to different initial states and trial functions: (a) upper stable state, buckling modes (ϕ = ϕ^b); (b) upper stable state, straight beam vibration modes (ϕ = ϕ^{sv}); (c) upper stable state, curved beam vibration modes (ϕ = ϕ^{cv}); (d) lower stable state, buckling modes (ϕ = ϕ^b); (e) lower stable state, straight beam vibration modes (ϕ = ϕ^{sv}); (f) lower stable state, curved beam vibration modes (ϕ = ϕ^{cv}).

Fig. 7 Ratio of the average axial (tension/compression) potential energy $\overline{U}_{\mathrm{s}}$ to the average bending potential energy $\overline{U}_{\mathrm{b}}$, evaluated at truncation order n = 3. The six subfigures correspond to different initial states and trial functions: (a) upper stable state, buckling modes ($\phi = \phi^{\mathrm{b}}$); (b) upper stable state, straight beam vibration modes ($\phi = \phi^{\mathrm{sv}}$); (c) upper stable state, curved beam vibration modes ($\phi = \phi^{\mathrm{cv}}$); (d) lower stable state, buckling modes ($\phi = \phi^{\mathrm{b}}$); (e) lower stable state, straight beam vibration modes ($\phi = \phi^{\mathrm{sv}}$); (f) lower stable state, curved beam vibration modes ($\phi = \phi^{\mathrm{cv}}$).

Fig. 8 Validation of the five-mode buckling-mode Galerkin predictions against finite element analysis (FEA) for motions starting from the upper stable state. (a) Dynamic response types: the background reproduces the numerical results from Fig. 6(a); superimposed markers denote FEA predictions (green circles: vacillating, yellow diamond: intra-well). Additional FEA points are placed in the subharmonic region enclosed by the red dashed frame. (b) Axial-to-bending energy ratio: the background shows the numerical results, while dots mark FEA-computed ratios. The red dashed frame highlights the region of elevated energy ratio beneath the subharmonic vacillating zone, confirming the importance of axial force.

Fig. 9 Effects of the initial arch height [h = 4.50 mm (0.177 in)] on the dynamic response predicted by the Galerkin method, starting from the upper stable state. (a)–(c) Third-order truncation using buckling, straight-beam vibration, and curved-beam vibration modes, respectively. (d)–(f) Fifth-order truncation with the same three mode sets.

Fig. 10 Effects of the viscous damping coefficient [$\hat{C}_d$ = 0.15 Pa·s (3.13×10^{-3} lbf·s/ft^2)] on the dynamic response predicted by the Galerkin method, starting from the upper stable state. (a)–(c) Third-order truncation using buckling, straight-beam vibration, and curved-beam vibration modes, respectively. (d)–(f) Fifth-order truncation with the same three mode sets.

Table Caption List

Figures and Tables

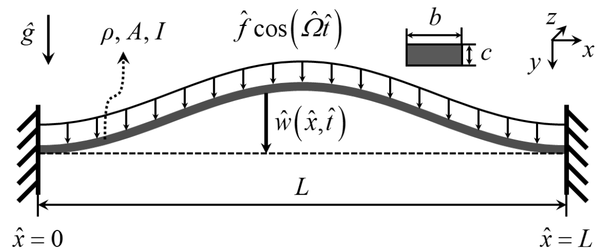

Fig. 1 Schematic of a clamped-clamped curved beam with its geometric parameters and under harmonic distributed excitation

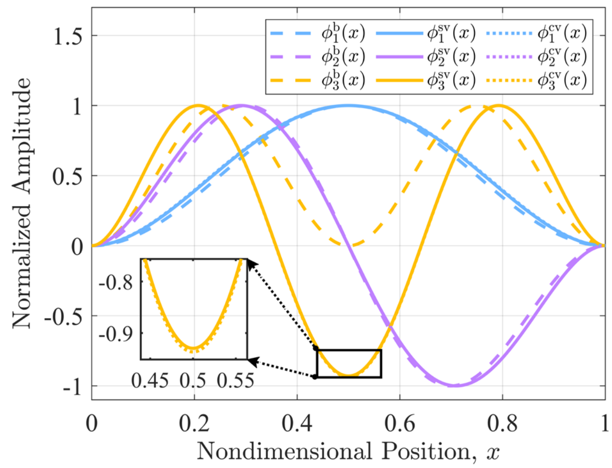

Fig. 2 Comparison of the first three buckling mode shapes (dashed lines), straight-beam vibration mode shapes (solid lines), and curved-beam vibration mode shapes (dotted lines), each normalized by its maximum value. In the main plot, the straight-beam and curved-beam vibration mode shapes are barely distinguishable. The inset provides a magnified view of the region where they diverge, highlighting the subtle difference between the straight- and curved-beam vibration modes.

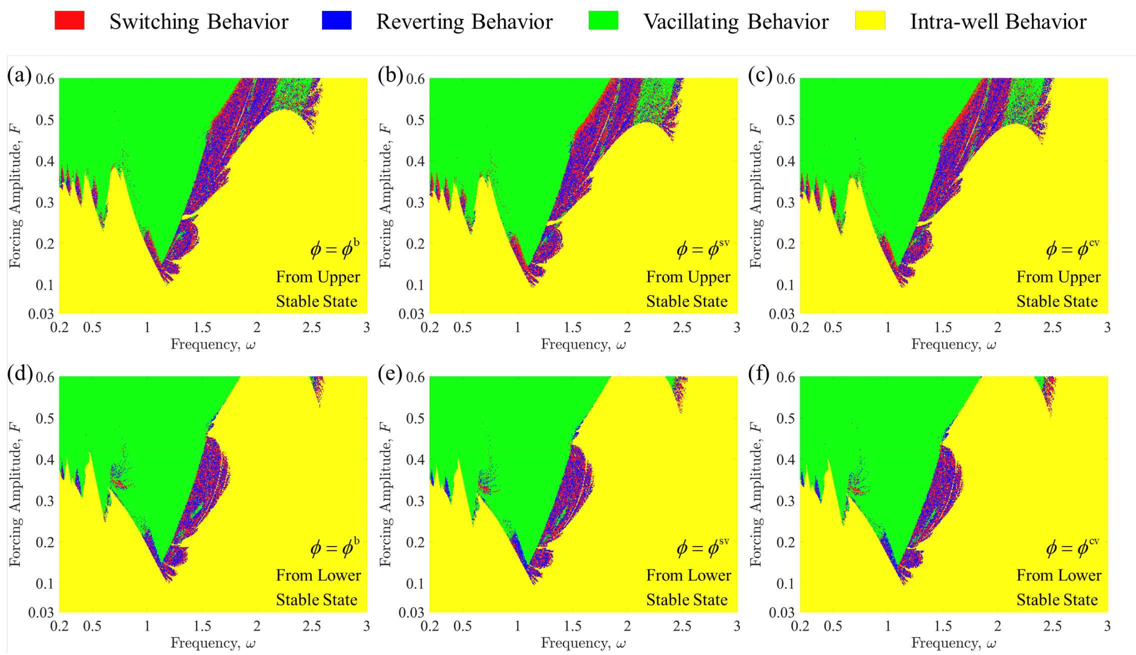

Fig. 3 Dynamic responses of the curved beam computed by the Galerkin method with truncation order *n* = 1. The six subfigures correspond to different initial states and trial functions: (a) upper stable state, buckling modes ($\boldsymbol{\phi} = \boldsymbol{\phi}^{b}$); (b) upper stable state, straight beam vibration modes ($\boldsymbol{\phi} = \boldsymbol{\phi}^{sv}$); (c) upper stable state, curved beam vibration modes ($\boldsymbol{\phi} = \boldsymbol{\phi}^{cv}$); (d) lower stable state, buckling modes ($\boldsymbol{\phi} = \boldsymbol{\phi}^{b}$); (e) lower stable state, straight beam vibration modes ($\boldsymbol{\phi} = \boldsymbol{\phi}^{sv}$); (f) lower stable state, curved beam vibration modes ($\boldsymbol{\phi} = \boldsymbol{\phi}^{cv}$).

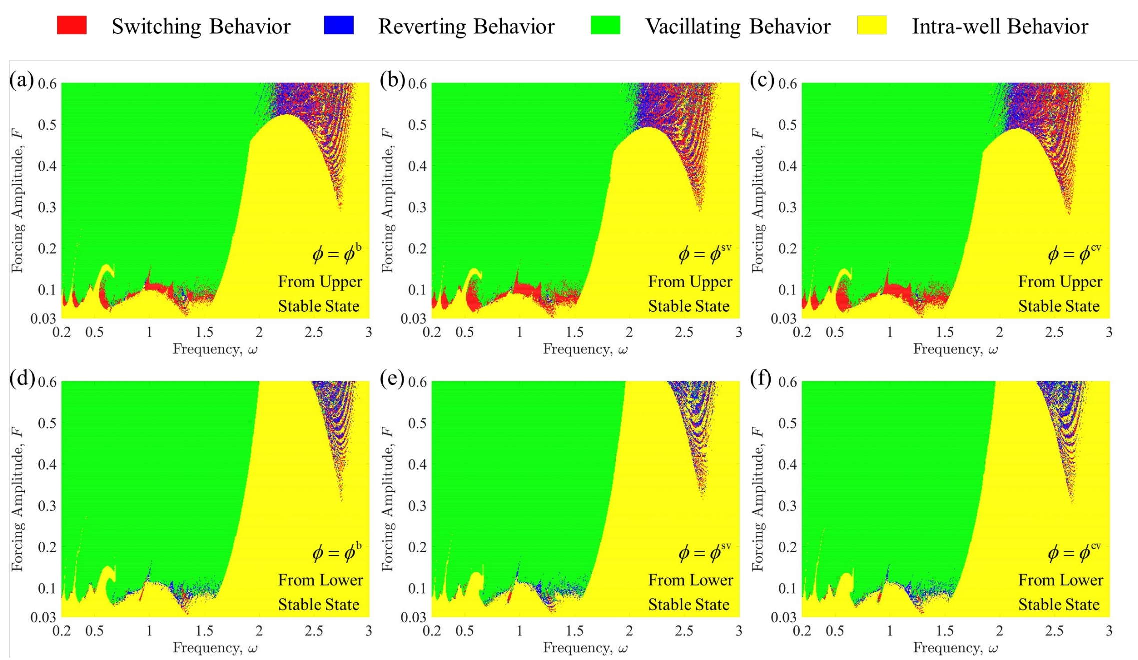

Fig. 4 Dynamic responses of the curved beam computed by the Galerkin method with truncation order *n* = 2. The six subfigures correspond to different initial states and trial functions: (a) upper stable state, buckling modes ($\phi = \phi^{b}$); (b) upper stable state, straight beam vibration modes ($\phi = \phi^{sv}$); (c) upper stable state, curved beam vibration modes ($\phi = \phi^{cv}$); (d) lower stable state, buckling modes ($\phi = \phi^{b}$); (e) lower stable state, straight beam vibration modes ($\phi = \phi^{sv}$); (f) lower stable state, curved beam vibration modes ($\phi = \phi^{cv}$).

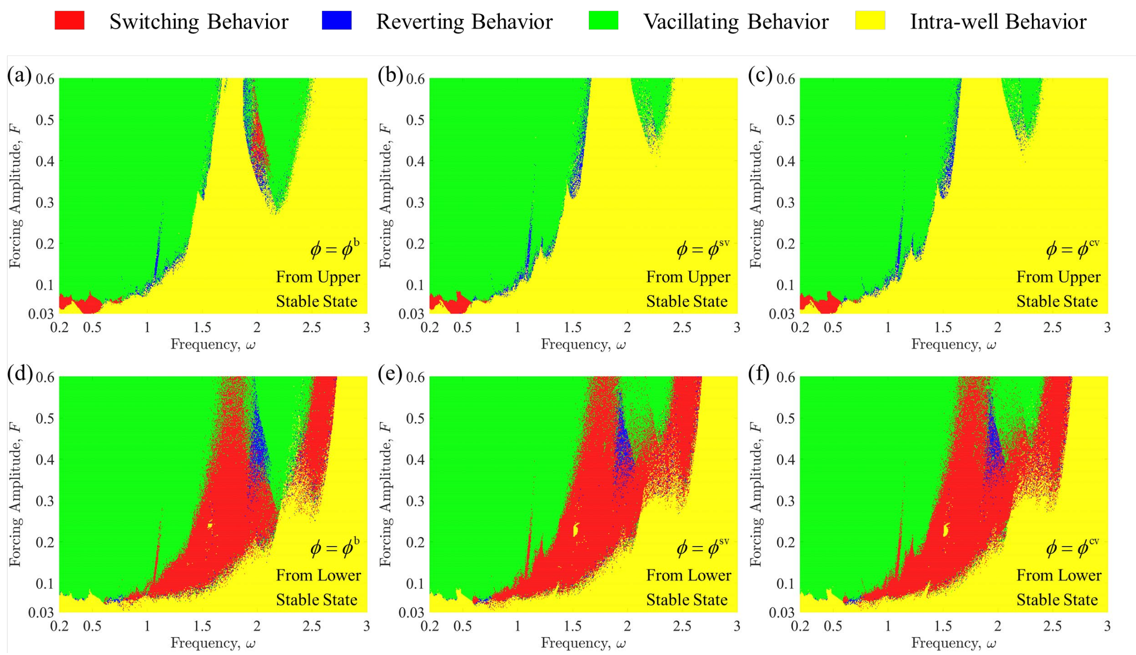

Fig. 5 Dynamic responses of the curved beam computed by the Galerkin method with truncation order *n* = 3. The six subfigures correspond to different initial states and trial functions: (a) upper stable state, buckling modes ($\phi = \phi^{b}$); (b) upper stable state, straight beam vibration modes ($\phi = \phi^{sv}$); (c) upper stable state, curved beam vibration modes ($\phi = \phi^{cv}$); (d) lower stable state, buckling modes ($\phi = \phi^{b}$); (e) lower stable state, straight beam vibration modes ($\phi = \phi^{sv}$); (f) lower stable state, curved beam vibration modes ($\phi = \phi^{cv}$).

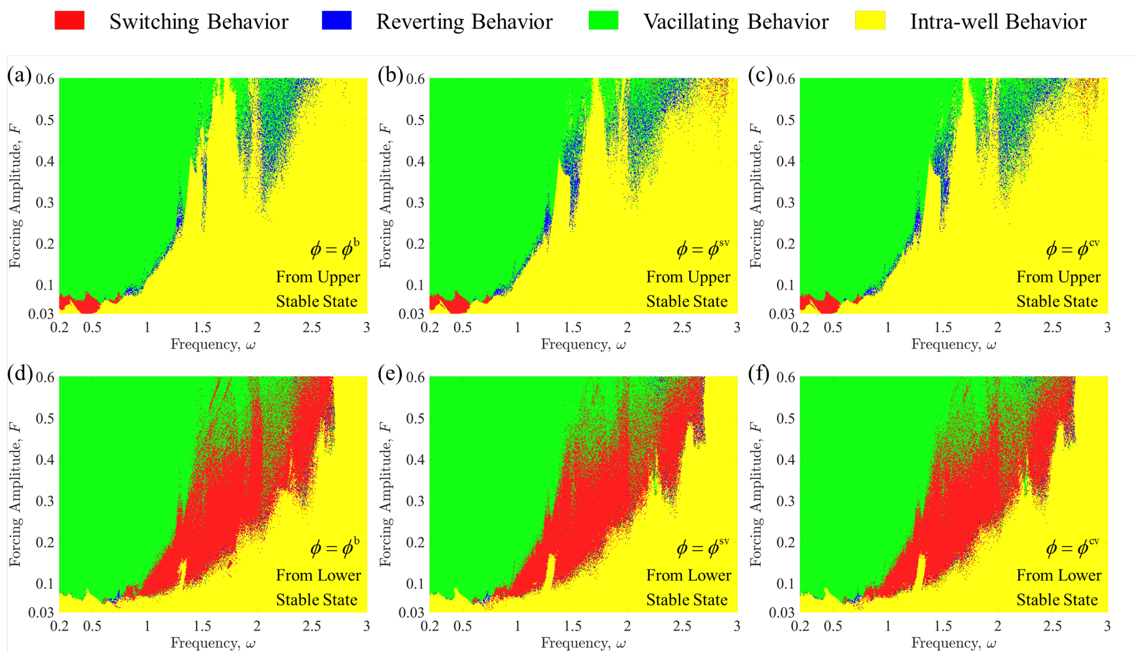

Fig. 6 **Dynamic responses of the curved beam computed by the Galerkin method with truncation order *n* = 5. The six subfigures correspond to different initial states and trial functions: (a) upper stable state, buckling modes ($\phi = \phi^{b}$); (b) upper stable state, straight beam vibration modes ($\phi = \phi^{sv}$); (c) upper stable state, curved beam vibration modes ($\phi = \phi^{cv}$); (d) lower stable state, buckling modes ($\phi = \phi^{b}$); (e) lower stable state, straight beam vibration modes ($\phi = \phi^{sv}$); (f) lower stable state, curved beam vibration modes ($\phi = \phi^{cv}$).**

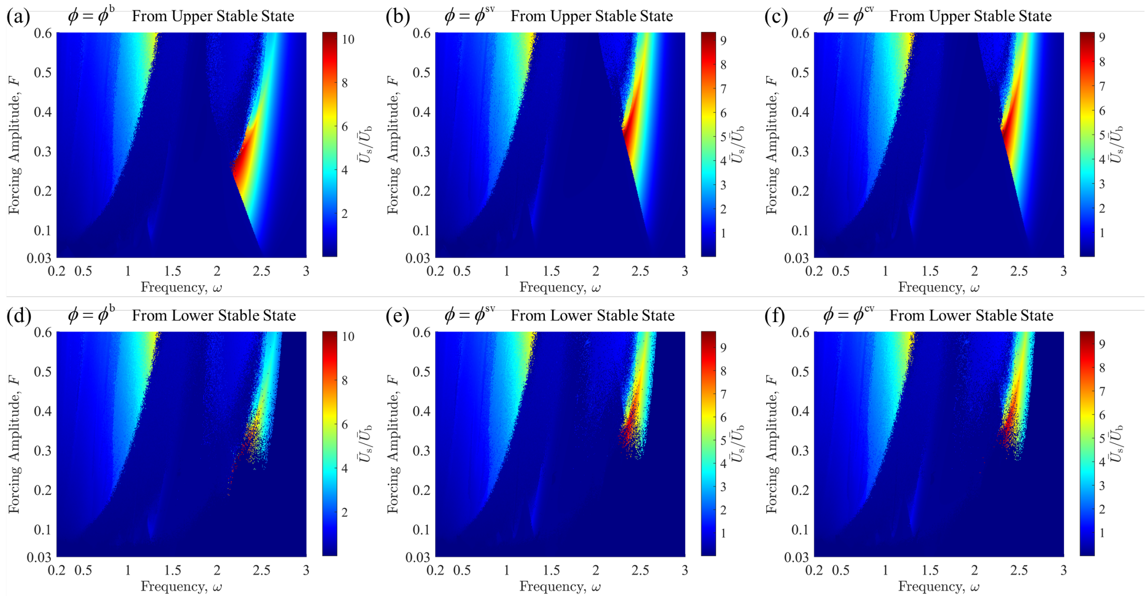

Fig. 7 Ratio of the average axial (tension/compression) potential energy $\overline{U}_{\mathrm{s}}$ to the average bending potential energy $\overline{U}_{\mathrm{b}}$, evaluated at truncation order *n* = 3. The six subfigures correspond to different initial states and trial functions: (a) upper stable state, buckling modes ($\phi = \phi^{\mathrm{b}}$); (b) upper stable state, straight beam vibration modes ($\phi = \phi^{\mathrm{sv}}$); (c) upper stable state, curved beam vibration modes ($\phi = \phi^{\mathrm{cv}}$); (d) lower stable state, buckling modes ($\phi = \phi^{\mathrm{b}}$); (e) lower stable state, straight beam vibration modes ($\phi = \phi^{\mathrm{sv}}$); (f) lower stable state, curved beam vibration modes ($\phi = \phi^{\mathrm{cv}}$).

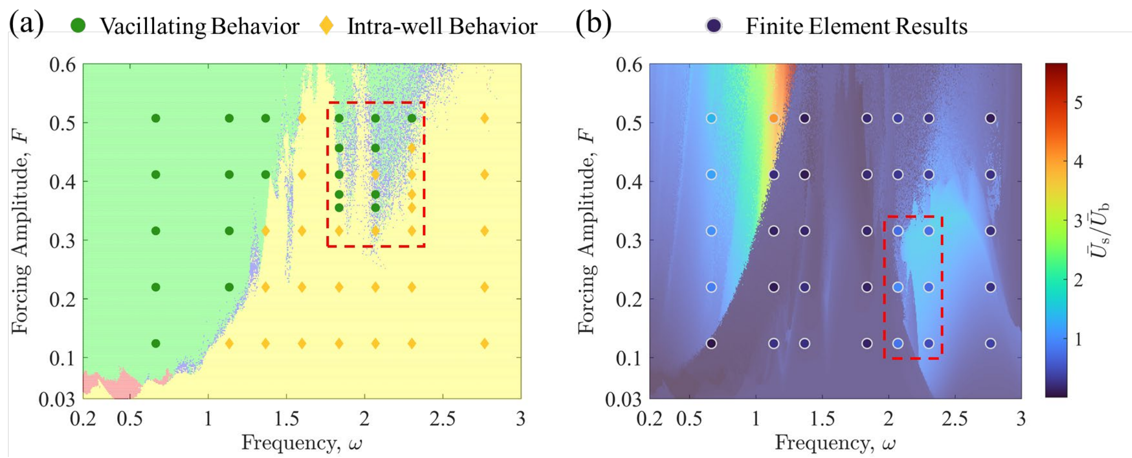

Fig. 8 Validation of the five-mode buckling-mode Galerkin predictions against finite element analysis (FEA) for motions starting from the upper stable state. (a) Dynamic response types: the background reproduces the numerical results from Fig. 6(a); superimposed markers denote FEA predictions (green circles: vacillating, yellow diamond: intra-well). Additional FEA points are placed in the subharmonic region enclosed by the red dashed frame. (b) Axial-to-bending energy ratio: the background shows the numerical results, while dots mark FEA-computed ratios. The red dashed frame highlights the region of elevated energy ratio beneath the subharmonic vacillating zone, confirming the importance of axial force.

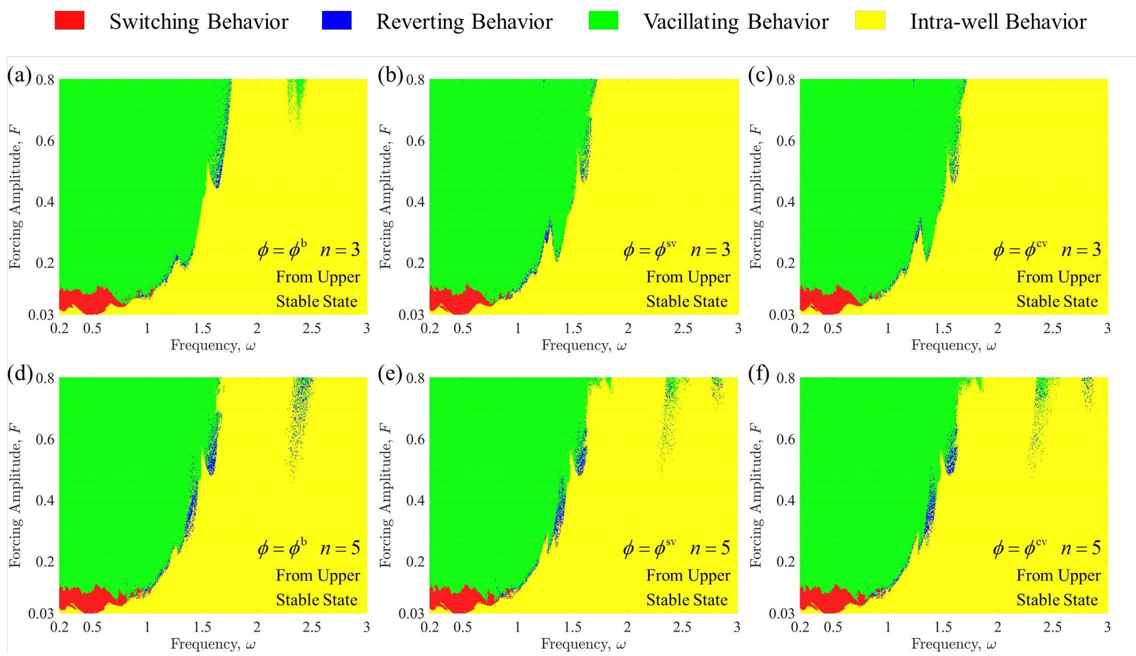

Fig. 9 Effects of the initial arch height [h = 4.50 mm (0.177 in)] on the dynamic response predicted by the Galerkin method, starting from the upper stable state. (a)–(c) Third-order truncation using buckling, straight-beam vibration, and curved-beam vibration modes, respectively. (d)–(f) Fifth-order truncation with the same three mode sets.

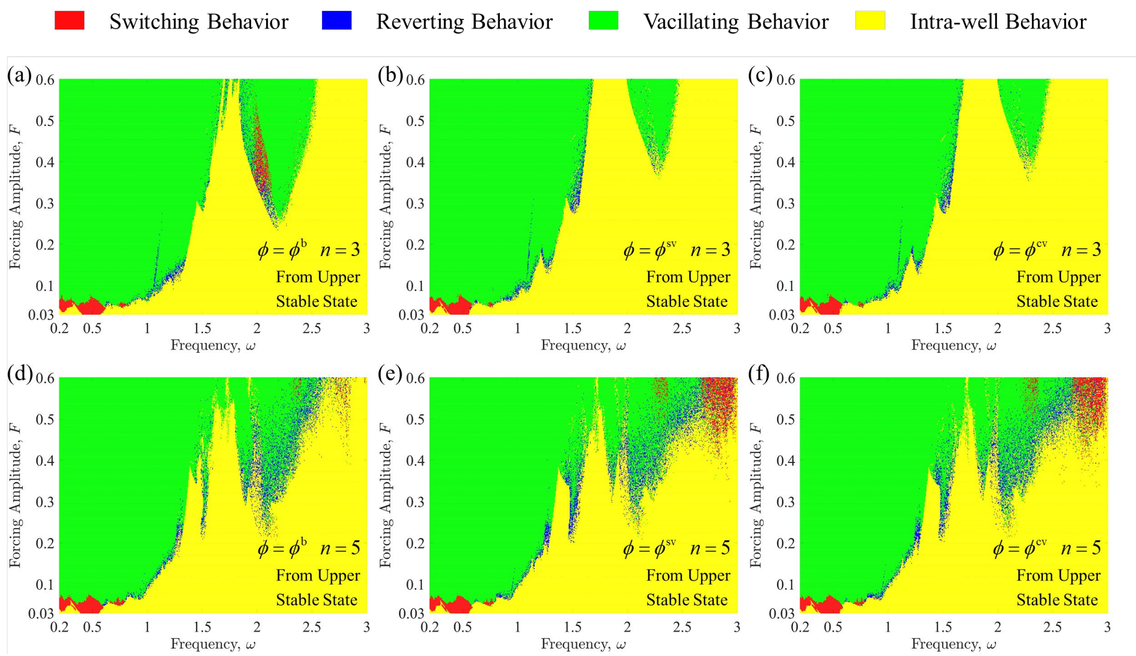

Fig. 10 Effects of the viscous damping coefficient [$\hat{C}_d$ = 0.15 Pa·s (3.13×10^{-3} lbf·s/ft^2)] on the dynamic response predicted by the Galerkin method, starting from the upper stable state. (a)–(c) Third-order truncation using buckling, straight-beam vibration, and curved-beam vibration modes, respectively. (d)–(f) Fifth-order truncation with the same three mode sets.

Table 1 Values of basic parameters

Item	Notation	Value
Beam span	L	0.06 m (2.36 in)
Beam width	b	0.01 m (0.394 in)
Beam thickness	c	1×10^{-3} m (0.0394 in)
Beam initial arch height	h	5.22×10^{-3} m (0.206 in)
Beam density	ρ	1082 kg/m^3 (67.55 lb/ft^3)
Young's modulus	E	0.74 MPa (107.3 psi)
Gravity acceleration	$\hat{g}$	9.8 m/s^2 (32.2 ft/s^2)
Viscous damping coefficient	$\hat{C}_\mathrm{d}$	0.2 Pa·s (4.18×10^{-3} lbf·s/ft^2)